Diagnostics of Interturn Short Circuits in PMSMs With Online Fault Indicators Estimation

Lukas Zezula ⬤, Matus Kozovsky ⬤, and Petr Blaha ⬤

Abstract—This article presents novel model-based diagnostics of interturn short circuits in permanent magnet synchronous machines that enable estimating fault location and its severity, even during transients. The proposed method utilizes recursive parametric estimation and model comparison approaches cast in a decision-making framework to track motor parameters and fault indicators from a machine's discrete-time model. The discrete-time prototype is derived from an advanced motor model that reflects the stator winding arrangement in a motor's case. The fault detection is then performed by tracking the changes in the estimated probability density function of the electrical parameters, using the Kullback–Leibler divergence. The fault location is subsequently evaluated by performing a recursive comparison of the predefined fault models in the different phases, utilizing a growing-window approach. Ultimately, a parametric estimation algorithm applied to the fault current model allows identifying the fault severity. The diagnostic algorithm has been validated via laboratory experiments, and its capabilities are compared with other approaches enabling severity estimation.

Index Terms—Discrete-time systems, fault detection, fault diagnosis, fault location, parameter estimation, permanent magnet motors, recursive estimation.

I. INTRODUCTION

PERMANENT magnet synchronous machines (PMSMs) are commonly used in robotics, industrial drives, and vehicular propulsions, where they must endure factors, such as vibration, moisture, and high temperatures. These effects constitute potential fault sources; thus, for example, a short circuit in the stator winding can be attributed to thermal degradation between the coil turns. Due to a low short-circuit impedance and an increased voltage amplified by coupled flux linkages, a significant fault current flows through the interturn short circuit (ISC), raising the current in the entire stator phase, generating heat, and further contributing to insulation material degradation [1], [2]. The resulting self-heating can ultimately lead to the machine's breakdown and eventual fire, producing a demand for responsive and dependable fault diagnostics and compensation.

Fault diagnostics recognize two main areas [3], [4]: signal analysis-based principles, which rely on expert knowledge [5], [6] or artificial intelligence [7], [8], and model-based diagnostics, which utilize different types of models and observers [9], [10]. Competing with established diagnostics requires novel algorithms to confront critical challenges as highlighted in [4]. These criteria suggest that novel diagnostics must be computationally efficient, capable of real-time operation, exclusively based on control structure signals, functionable even during transient states, and capable of extracting fault indicators in each feasible operating point, all without additional hardware extensions. Attaining such demands with a single diagnostic algorithm enables the advanced fault mitigation methods [11], [12], [13], [14] to function, thus enhancing the fault-tolerant control capabilities.

Currently, most ISC diagnostic algorithms, which aim to extract fault indicators, such as severity and location, do not adhere to the abovementioned requirements, as they do not operate during transients [15], [16], [17], [18], [19] and need additional hardware [20]. The neural network-based algorithm [21] comes closest to meeting the specified criteria; yet, as the algorithm was not implemented into an embedded device, its efficiency and hardware requirements remain unknown. This article aims to design an efficient parametric estimation-based diagnostic algorithm that facilitates rapid detection of ISCs, along with precise extraction of their locations and severity, even during transients and different operating conditions; thus, the critical requirements of modern diagnostics are addressed. Unlike the existing parametric estimation-based diagnostic methods [22], [23], our solution exploits a discrete-time model and employs techniques cast in a decision-making framework [24], [25], [26], [27].

The Bayesian approach offers several advantages over the traditional parametric estimation methods (such as the prediction error ones [28]); for instance, the approach mitigates the problems associated with the estimator efficiency, unbiasedness, and credibility interval. In addition, the Bayes-based algorithms

naturally incorporate regularization effects, helping to prevent overfitting and to enhance the model generalization. Furthermore, by providing uncertainty estimates through posterior distribution, the framework allows data-informed decision-making applicable to fault diagnostics.

The rest of this article is organized as follows. Section II focuses on the discrete-time modeling of a PMSM with an ISC. Section III discusses the algorithm design and its applicability. The diagnostic algorithm is then validated in Section IV via laboratory experiments. Finally, Section V concludes this article.

II. DISCRETE-TIME MODEL

The mathematical modeling of PMSMs under an ISC was previously described by Zezula [29]. Considering a motor with close rotor reference frame inductances $L_d = L_q = L_s$, the mathematical model reads

$$
\begin{bmatrix} i_\alpha \\ i_\beta \end{bmatrix} = \begin{bmatrix} 1 & 0 & 1 & 0 \\ 0 & 1 & 0 & 1 \end{bmatrix} \begin{bmatrix} i_{\alpha,h} & i_{\beta,h} & i_{\alpha,f} & i_{\beta,f} \end{bmatrix}^T
$$

(1a)

$$
\frac{d}{dt} \begin{bmatrix} i_{\alpha,h} \\ i_{\beta,h} \end{bmatrix} = -\frac{R_s}{L_s} \begin{bmatrix} i_{\alpha,h} \\ i_{\beta,h} \end{bmatrix} + \frac{1}{L_s} \begin{bmatrix} u_\alpha \\ u_\beta \end{bmatrix} + \frac{\omega_e \lambda_{\text{pm}}}{L_s} \begin{bmatrix} \sin(\theta_e) \\ -\cos(\theta_e) \end{bmatrix}
$$

(1b)

$$
\frac{d}{dt} \begin{bmatrix} i_{\alpha,f} \\ i_{\beta,f} \end{bmatrix} = -\frac{R_f^*}{L_f} \begin{bmatrix} i_{\alpha,f} \\ i_{\beta,f} \end{bmatrix} + \frac{x_f^2}{n_s^2 L_f} \Phi \begin{bmatrix} u_\alpha \\ u_\beta \end{bmatrix}
$$

(1c)

where i_α, i_β and u_α, u_β are the stator reference frame currents and voltages, respectively, $i_{\alpha,h}$, $i_{\beta,h}$ and $i_{\alpha,f}$, $i_{\beta,f}$ denote the contributions by the healthy model (1b) and the short-circuit current components (1c) to the stator reference frame ($\alpha - \beta$) currents, respectively, and ω_e, θ_e stand for the electrical angular velocity and angle, respectively. The parameters R_s, L_s, and λ_{pm} represent the equivalent stator resistance, inductance, and permanent magnet flux linkage. In (1c), the parameters R_f^* and L_f are set as in

$$
R_f^* = (1 - 3n_p) R_s \frac{x_f^2}{n_s^2} + 3n_p R_s \frac{x_f}{n_s} + 3R_f
$$

(2a)

$$
L_f = 2 \frac{x_f^2 n_p (n_s - 1)}{n_s^2} L_s
$$

(2b)

where the constants n_p and n_s are related to the stator winding connection and distribution inside the motor's case, respectively. Generally, n_p describes the number of parallel-connected stator winding branches, and n_s stands for the number of coils in series in each stator branch. The described stator winding connection that contains an ISC is shown in Fig. 1.

The fault-related parameters R_f and x_f then stand for the short-circuit resistance and fault severity, respectively, quantifying the proportion of shorted turns to total turns within the coil segment.

The short circuits in the different stator phases are then distinguished in (1c) by the matrix Φ, described as in

$$
\Phi = \begin{bmatrix} 1 + \cos(\phi) & -\sin(\phi) \\ -\sin(\phi) & 1 - \cos(\phi) \end{bmatrix}
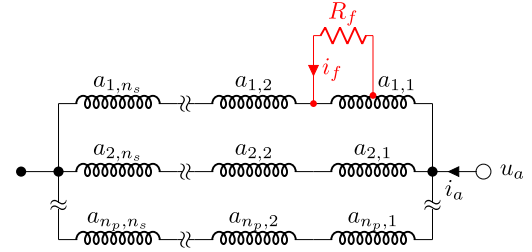$$

(3)

Fig. 1. Phase a winding under an ISC fault.

where $\phi = \{0, 2\pi/3, -2\pi/3\}$, if the ISC is in phase $\{a, b, c\}$. The relationship between the fault current i_f and its contributions $i_{\alpha,f}$ and $i_{\beta,f}$ to the $\alpha - \beta$ currents reads

$$
i_{\alpha,f} = \frac{2x_f}{3n_s} \cos\left(\frac{\phi}{2}\right) i_f \quad i_{\beta,f} = -\frac{2x_f}{3n_s} \sin\left(\frac{\phi}{2}\right) i_f.
$$

(4)

As the parametric estimation methods mainly rely on discrete-time models [28], the continuous-time equations (1b) and (1c) must be discretized, necessitating analysis of the input signals between the sampling intervals. Voltage control in the stator variables (abc) is achieved through inverter switching, also reflected in $\alpha - \beta$ due to the linear Clarke's transformation. However, adjusted current sampling allows suppressing the pulsewidth modulation distortion, enabling description with constant voltages over the sampling period. We have

$$
\begin{aligned}
u_\alpha(t) &= u_\alpha(k-1) & (k-1)T_s \leq t < kT_s \\
u_\beta(t) &= u_\beta(k-1) & (k-1)T_s \leq t < kT_s
\end{aligned}
$$

(5)

where t represents the time, T_s denotes the sampling period, and k stands for the current step of the discrete-time equivalent. In scenarios involving PMSMs, the angle is sampled concurrently with the stator currents. The frequency at which the angle is sampled is essential, as it controls its availability in the rotor reference frame transformation. Therefore, the sampling rate tailored to the dynamics of the current loop is excessively high for a slower mechanical subsystem, and only minimal velocity variations occur during one sampling period, enabling the following velocity $\omega_e(t) = \bar{\omega}_e$ approximation:

$$
\bar{\omega}_e = \frac{\omega_e(k) + \omega_e(k-1)}{2} \quad (k-1)T_s \leq t < kT_s.
$$

(6)

The approximation assumes that $\omega_e(t)$ is constant over the sampling period, leading to the linear angle. Thus, by approximating the inputs (5) and (6), the discrete-time equivalent of the shorted motor's model formulated as the linear time-invariant system (1a)–(1c) reads (7a)–(8c), where $\sigma = \{\alpha, \beta\}$, (7a), and (7b) describe the motor's behavior before the short circuit, and (8a)–(8c) express the distortion in the stator reference frame currents that results from an ISC.

III. DIAGNOSTIC ALGORITHM

The diagnostic algorithm covers the following three parts.

1) *Tracking the healthy machine behavior:* To estimate the series resistance, inductance, and permanent magnet flux linkage (motor parameters).

2) *Fault detection:* Determining whether and when a fault has occurred.

3) *Estimating the fault indicators:* Such as the fault severity and location (which phase is shorted).

A. Tracking the Healthy Machine Behavior

Typically, vector control is implemented in driving alternate current machines, employing several closed control loops to regulate the angular velocity and electromagnetic torque effectively. Due to the closed-loop control, the model's inputs have limited persistence. For example, in the steady state, the stator reference frame voltages are harmonic signals whose frequency corresponds to the electrical angular velocity, enabling estimation of not more than two parameters in the model [28]. Therefore, it is desirable to identify the electrical parameters of the motor out of (7a) and (7b) before a fault occurs. Once a short circuit has been detected, the estimated parameters become usable as fixed values instead of retracking, resulting in reduced persistence requirements for the input signals.

Several facts have to be considered when selecting an estimation algorithm. First, in the steady state, the inputs possess a persistence to estimate only two parameters; however, the healthy model has three parameters. The information obtained during the transients must therefore be used to identify the parameters correctly. Consequently, an estimation strategy with fixed exponential forgetting would result in inaccurate parameter assessment in the steady state. In contrast, the electrical parameters of a motor are generally time varying; for instance, the inductance decreases with increasing current due to the occurrence of magnetic saturation. Exponential forgetting thus accelerates the parameter adjustment. The parametric estimation algorithm with variable exponential forgetting described by Dokoupil and Václavek [24] fulfills the contradictory requirements of exponential forgetting. Moreover, the constraints presented in [24] make the estimator robust to poor system excitation.

As shown in (7a) and (7b), the estimation uses a pseudolinear model, where $v_\alpha(k, k-1)$ and $v_\beta(k, k-1)$ are calculated based on the previously identified $\Theta_{h,\alpha}$ and $\Theta_{h,\beta}$. As a motor may exhibit an asymmetry in the stator windings, updating $v_\alpha(k, k-1)$ and $v_\beta(k, k-1)$ with the corresponding parameters $\Theta_{h,\alpha}$ and $\Theta_{h,\beta}$ is crucial; importantly, the parameters

---

Algorithm 1: Estimating the Electrical Parameters.

1: **Initialization:**
2:    Set up the constrained terms Ξ, tuning factor $\zeta \in (0, 1)$, and lower bound of the forgetting factor $\alpha \in (0, 1)$. The applied initialization: $\Xi = 0.7\,\mathbf{I}^{3\times3}$, $\zeta = 0.42$, $\alpha = 0.95$.
3:    $init\_done \leftarrow false$
4:    **if** $\omega_e^*(k-1) \neq \omega_e^*(k)$ **and** $\bar{\omega}_e == 0$ **then**
5:      /* Start if the velocity is zero and its setpoint ω_e^* has changed (use transients for the initial guess) */
6:      $init\_done \leftarrow true$
7:    **end if**
8: **Electrical parameter estimation:**
9:    **while** $|\bar{\omega}_e| > 0$ **and** $init\_done$ **do**
10:      Calculate $v_\alpha(k, k-1)$ and $v_\beta(k, k-1)$ as in (7b), using the current $\bar{\omega}_e$ (6) and parameters estimated in the previous step $\Theta_{h,\alpha}(k-1)$ and $\Theta_{h,\beta}(k-1)$.
11:      Execute the step of two independently running algorithms [24] to obtain the current estimations of the electrical parameters $\Theta_{h,\alpha}(k)$ and $\Theta_{h,\beta}(k)$ out of the $\alpha - \beta$ currents model (7a).
12: **end while** .

---

are estimated independently. A similar statement holds also for evaluating transformations (8b) and (8c). In conventional practice, ensuring the stability of a pseudolinear estimator involves establishing a dependable initial parameter guess. However, if $\bar{\omega}_e \to 0$, the signals $v_\alpha(k, k-1)$ and $v_\beta(k, k-1)$ have a negligible impact on $i_{\alpha,h}(k)$ and $i_{\beta,h}(k)$. Consequently, the initial parameters can be arbitrarily chosen if the parametric estimation initiates in the operating point close to $\omega_e = 0$. The parameter tracking algorithm reads Algorithm 1.

B. Fault Detection

The algorithm presented by Dokoupil and Václavek [24] estimates the statistics of the identified parameter's Normal–Wishart ($\mathcal{NW}$) probability distribution function (PDF) $f(\Theta, d) = \mathcal{N}(\Theta, \mathbf{V}^{-1}/d)\mathcal{W}(\Sigma, \nu)$, where Θ stands for the vector of identified parameters, $\mathbf{V}$ is the information matrix—inverse of a covariance matrix normalized by the noise precision d, Σ denotes

$$i_{\sigma,h}(k) = \begin{bmatrix} i_{\sigma,h}(k-1) & u_\sigma(k-1) & v_\sigma(k, k-1) \end{bmatrix} \begin{bmatrix} e^{-\frac{R_s}{L_s}T_s} & \frac{1-e^{-\frac{R_s}{L_s}T_s}}{R_s} & \frac{\lambda_{pm}}{L_s} \end{bmatrix}^T = \mathbf{h}_{h,\sigma}^T \Theta_{h,\sigma} \tag{7a}$$

$$\begin{bmatrix} v_\alpha(k, k-1) \\ v_\beta(k, k-1) \end{bmatrix} = \frac{\bar{\omega}_e}{\frac{R_s^2}{L_s^2} + \bar{\omega}_e^2} \left(e^{-\frac{R_s}{L_s}T_s} \begin{bmatrix} \cos(\theta_e(k-1)) & -\sin(\theta_e(k-1)) \\ \sin(\theta_e(k-1)) & \cos(\theta_e(k-1)) \end{bmatrix} - \begin{bmatrix} \cos(\theta_e(k)) & -\sin(\theta_e(k)) \\ \sin(\theta_e(k)) & \cos(\theta_e(k)) \end{bmatrix} \right) \begin{bmatrix} \bar{\omega}_e \\ \frac{R_s}{L_s} \end{bmatrix} \tag{7b}$$

$$\begin{bmatrix} \tilde{i}_\alpha(k) \\ \tilde{i}_\beta(k) \end{bmatrix} = e^{-\frac{R_f^*}{L_f}T_s} \begin{bmatrix} \tilde{i}_\alpha(k-1) \\ \tilde{i}_\beta(k-1) \end{bmatrix} + \frac{x_f^2}{n_s^2} \frac{1-e^{-\frac{R_f^*}{L_f}T_s}}{R_f^*} \Phi \begin{bmatrix} \tilde{u}_\alpha(k-1) \\ \tilde{u}_\beta(k-1) \end{bmatrix} \tag{8a}$$

$$\tilde{i}_\sigma(k) = i_\sigma(k) - \begin{bmatrix} i_\sigma(k-1) & u_\sigma(k-1) & v_\sigma(k, k-1) \end{bmatrix} \Theta_{h,\sigma} \tag{8b}$$

$$\tilde{u}_\sigma(k) = u_\sigma(k) - e^{-\frac{R_s}{L_s}T_s} u_\sigma(k-1) \tag{8c}$$

the least square reminder, and ν represents the number of the degrees of freedom. After an ISC occurs, the stator reference frame currents are distorted by the short-circuit current contributions, as in (8a)–(8c). The rapid change in the measured currents is then reflected in the Normal–Wishart statistics updated in each step, and the PDF does not fit its previous estimate. The difference between PDFs is typically assessed via the Kullback–Leibler divergence. As mentioned by Dokoupil and Václavek [24], the divergence between the two Normal–Wishart PDFs $f_1(\Theta, d)$ and $f_2(\Theta, d)$ reads

$$\mathcal{D}_{\text{KL}}\left(f_1(\Theta, d) \| f_2(\Theta, d)\right) = \frac{1}{2}\ln\left(\frac{|\mathbf{V}_1|}{|\mathbf{V}_2|}\right) + \frac{1}{2}\text{tr}\left(\mathbf{V}_2 \mathbf{V}_1^{-1}\right)$$

$$+ \ln\left(\frac{\Gamma\left(\frac{\nu_2}{2}\right)}{\Gamma\left(\frac{\nu_1}{2}\right)}\right) - \frac{n}{2} + \frac{\nu_2}{2}\ln\left(\frac{\Sigma_1}{\Sigma_2}\right) - \frac{\nu_1}{2}\left(\frac{\Sigma_1 - \Sigma_2}{\Sigma_1}\right)$$

$$+ \frac{\nu_1}{2\Sigma_1}\left(\Theta_1 - \Theta_2\right)^T \mathbf{V}_2 \left(\Theta_1 - \Theta_2\right) + \frac{\nu_1 - \nu_2}{2}\Psi\left(\frac{\nu_1}{2}\right) \quad (9)$$

where n stands for the dimension of the square matrix $\mathbf{V}^{n \times n}$, and the gamma and digamma functions are replaced by their asymptotic approximations as in

$$\Gamma\left(\frac{\nu}{2}\right) \approx e^{-\frac{\nu}{2}}\left(\frac{\nu}{2}\right)^{\frac{\nu-1}{2}}\sqrt{2\pi} \quad \Psi\left(\frac{\nu}{2}\right) \approx \ln\left(\frac{\nu}{2}\right) - \frac{1}{\nu}. \quad (10)$$

If the motor winding does not contain an ISC, it follows the healthy model (7a) and (7b), and the estimation of the parameters' PDF converges to an exact PDF. The convergence assumption is described as follows:

$$\varepsilon\left[\mathcal{D}_{\text{KL}}\left(f_e \| f_c\right)\right] \leq \varepsilon\left[\mathcal{D}_{\text{KL}}\left(f_e \| f_p\right)\right] \quad (11)$$

where $\varepsilon[x]$ is the expectation of x, f_e denotes the exact PDF of the model's parameters, f_c represents the currently estimated parameters' PDF, and f_p is the previously estimated parameters' PDF. The divergence expectations (11) can be then modeled by the following convex combinations of admissible realizations:

$$\varepsilon\left[\mathcal{D}_{\text{KL}}\left(f_e \| f_c\right)\right] = \bar{p}\underbrace{\mathcal{D}_{\text{KL}}\left(f_c \| f_c\right)}_{0} + p\mathcal{D}_{\text{KL}}\left(f_p \| f_c\right)$$

$$\varepsilon\left[\mathcal{D}_{\text{KL}}\left(f_e \| f_p\right)\right] = \bar{p}\mathcal{D}_{\text{KL}}\left(f_c \| f_p\right) + p\underbrace{\mathcal{D}_{\text{KL}}\left(f_p \| f_p\right)}_{0} \quad (12)$$

where $\bar{p} = 1 - p$ expresses the probability that f_c is the best projection of f_e, and p represents the probability that f_p is the best projection of f_e. Suppose the parametric estimation algorithm defined in Section III-A has been running for a long time; the PDFs f_c and f_p then nearly correspond to each other, and the inequality in (11) can be replaced with equality. The probability p then writes

$$p = \frac{\mathcal{D}_{\text{KL}}\left(f_c \| f_p\right)}{\mathcal{D}_{\text{KL}}\left(f_c \| f_p\right) + \mathcal{D}_{\text{KL}}\left(f_p \| f_c\right)} \approx 0.5. \quad (13)$$

Conversely, if a short circuit occurs, the uncertainty of the currently estimated PDF f_c increases compared with the previously estimated PDF f_p. Thus, the inequality (11) does not apply, and the probability p grows above 0.5 (the previously estimated PDF f_p describes the exact PDF f_e more reliably than f_c). The fault presence is then indicated by an excess of p, the probability

Algorithm 2: Detecting the Fault Occurrence.

1:    **Initialization:**
2:    Set up the length of the time delay (in steps) δ and the uncertainty interval ξ. The applied initialization: $\delta = 10, \xi = 0.015$.
3:    $ISC \leftarrow false$
4:    **Fault detection:**
5:    **while** not(ISC) **do**
6:      /* For both estimated models $\sigma = \{\alpha, \beta\}$: */
7:      Acquire the statistics $\Theta_{h,\sigma}(k - \delta)$, $\mathbf{V}_\sigma(k - \delta)$, $\nu_\sigma(k - \delta)$, and $\Sigma_\sigma(k - \delta)$ of the previously estimated PDF $f_{p,\sigma}$.
8:      Acquire the statistics $\Theta_{h,\sigma}(k)$, $\mathbf{V}_\sigma(k)$, $\nu_\sigma(k)$, and $\Sigma_\sigma(k)$ of the currently estimated PDF $f_{c,\sigma}$.
9:      Evaluate $\mathcal{D}_{KL}(f_{c,\sigma} \| f_{p,\sigma})$ and $\mathcal{D}_{KL}(f_{p,\sigma} \| f_{c,\sigma})$ as in (9) and the probability p_σ as in (13).
10:     Calculate the joint probability $p_{\alpha \cap \beta} = p_\alpha p_\beta$.
11:     **if** $p_{\alpha \cap \beta} > 0.25 + \xi$ **then**
12:      $ISC \leftarrow true$ and $\Theta_{h,\sigma}(k) \leftarrow \Theta_{h,\sigma}(k - \delta)$
13:     **end if**
14:    **end while** .

rising above the defined value greater than 0.5. As the required statistics are independently estimated for both of the $\alpha - \beta$ model parts in Algorithm 1, we investigate the surpassing of the joint probability beyond 0.25. The fault detection Algorithm 2

C. Estimating the Fault Indicators

As seen in (8a), the faults in the different stator phases are distinguished by the matrix Φ, defined in (3). Since ϕ can achieve only three values (0, $2\pi/3$, and $-2\pi/3$), identifying ϕ by a parametric estimation algorithm is unnecessary. Instead, note that the short-circuit current contributions mentioned in (4) depend on $\cos(\phi/2)$ and $-\sin(\phi/2)$. A similar dependence also holds for the remainders $\tilde{i}_\alpha$ and $\tilde{i}_\beta$. Then, the following transformation can be evaluated:

$$\begin{bmatrix} \hat{\tilde{i}}_f(k, \hat{\phi}) \\ \hat{\tilde{i}}_0(k, \hat{\phi}) \end{bmatrix} = \begin{bmatrix} \cos\left(\frac{\hat{\phi}}{2}\right) & -\sin\left(\frac{\hat{\phi}}{2}\right) \\ \sin\left(\frac{\hat{\phi}}{2}\right) & \cos\left(\frac{\hat{\phi}}{2}\right) \end{bmatrix} \begin{bmatrix} \tilde{i}_\alpha(k) \\ \tilde{i}_\beta(k) \end{bmatrix}$$

$$= \mathbf{R}(\hat{\phi})\begin{bmatrix} \cos\left(\frac{\phi}{2}\right) \\ -\sin\left(\frac{\phi}{2}\right) \end{bmatrix}\tilde{i}_f(k) = \begin{bmatrix} \cos\left(\frac{\hat{\phi}-\phi}{2}\right) \\ -\sin\left(\frac{\hat{\phi}-\phi}{2}\right) \end{bmatrix}\tilde{i}_f(k) \quad (14)$$

where $\hat{\phi}$ stands for the guess of the parameter ϕ. If $\hat{\phi} = \phi$, then $\hat{\tilde{i}}_f(k, \phi) = \tilde{i}_f(k)$ and $\hat{\tilde{i}}_0(k, \phi) = 0$. Hence, the fault location can be determined by comparing the probabilities of the hypotheses $\hat{\tilde{i}}_{0,a}(k, \phi_a = 0) = 0$, $\hat{\tilde{i}}_{0,b}(k, \phi_b = 2\pi/3) = 0$, and $\hat{\tilde{i}}_{0,c}(k, \phi_c = -2\pi/3) = 0$. An algorithm to assign the probabilities of Kalman filters based on the Bayesian inference was derived by Dokoupil et al. [25]. As comparing a measured signal with zero value is an application case of Kalman filtering, the probabilities of the previously mentioned hypotheses can be assigned as follows:
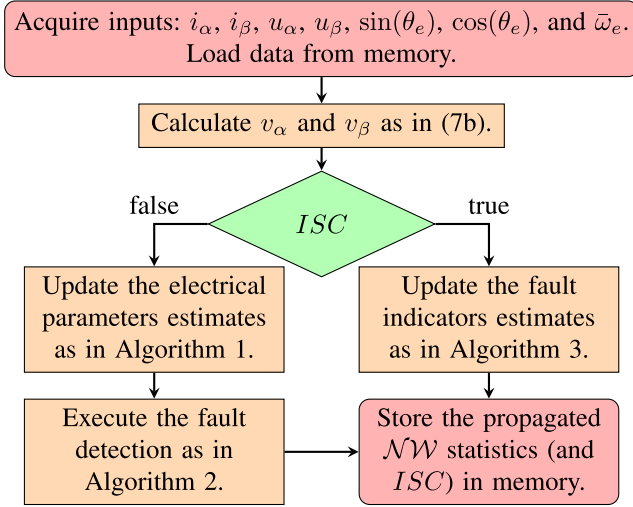
Fig. 2. One step in the fault diagnostic procedure.

$$p_j(k+1) =$$

$$\frac{\Sigma_j(k)^{-\frac{1}{2}}\left(1 + \frac{\hat{i}_{0,j}(k+1,\phi_j)^2}{\Sigma_j(k)}\right)^{-\frac{\nu(k)+1}{2}} p_j(k)}{\sum_{i\in\{a;b;c\}} \Sigma_i(k)^{-\frac{1}{2}}\left(1 + \frac{\hat{i}_{0,i}(k+1,\phi_i)^2}{\Sigma_i(k)}\right)^{-\frac{\nu(k)+1}{2}} p_i(k)} \quad (15)$$

where $\Sigma_j(k+1)$ and $\nu(k+1)$ are updated as in

$$\Sigma_j(k+1) = \Sigma_j(k) + \hat{i}_{0,j}(k+1,\phi_j)^2$$
$$\nu(k+1) = \nu(k) + 1. \quad (16)$$

The information on the fault location can then be utilized to form a difference equation describing $\tilde{i}_f$. We have

$$\tilde{i}_f(k) = \cos\left(\frac{\phi}{2}\right)\tilde{i}_\alpha(k) - \sin\left(\frac{\phi}{2}\right)\tilde{i}_\beta(k) \quad (17a)$$

$$\tilde{u}_f(k) = \cos\left(\frac{\phi}{2}\right)\tilde{u}_\alpha(k) - \sin\left(\frac{\phi}{2}\right)\tilde{u}_\beta(k) \quad (17b)$$

$$\tilde{i}_f(k) = \begin{bmatrix}\tilde{i}_f(k-1) & \tilde{u}_f(k-1)\end{bmatrix}\underbrace{\begin{bmatrix} e^{-\frac{R_f^*}{L_f}T_s} \\ 2\frac{x_f^2}{n_s^2}\frac{1-e^{-\frac{R_f^*}{L_f}T_s}}{R_f^*}\end{bmatrix}}_{\Theta_f}. \quad (17c)$$

Note that, according to (2a) and (2b), by using the estimated Θ_f, the parameters x_f and R_f cannot be distinguished from each other. In this article, the fault severity is therefore estimated assuming a zero ISC resistance $x_f(R_f = 0\,\Omega)$. Furthermore, as the computation of x_f depends on R_s, separately estimated for both of the $\alpha - \beta$ components, we are transforming R_s from $\alpha - \beta$ to abc and utilizing the output linked to the fault location ϕ. The fault indicators are estimated by the following algorithm.

Fig. 2 then depicts one step of the diagnostic algorithm executed in each sampling period.

D. Applicability of the Diagnostic Algorithm

The designed diagnostics are primarily dedicated to PMSMs with concentrated windings and close rotor reference frame inductances (surface-mounted PMSMs). By reflecting a universal

---

Algorithm 3: Estimating the Fault Indicators.

1: **Initialization:**
2:   Set up the initial probabilities $p_a = 1/3$, $p_b = 1/3$, and $p_c = 1/3$, least square reminders $\Sigma_a = \Sigma_b = \Sigma_c = 1$, and number of the degrees of freedom $\nu = 1$.
3:   Initialize the parametric estimation algorithm [24] similarly to Algorithm 1. The applied initialization: $\Xi = \mathbf{I}^{2\times 2}$, $\zeta = 0.05$, $\alpha = 0.95$.
4: **Fault indicator estimation:**
5: **while** $|\bar{\omega}_e| > 0$ **do**
6:   Calculate $\hat{i}_{0,a}(k,\phi_a)$, $\hat{i}_{0,b}(k,\phi_b)$, and $\hat{i}_{0,c}(k,\phi_c)$ as in (14) and update the probabilities p_a, p_b, p_c as in (15).
7:   Choose $\hat{\phi} = \phi$ correspondingly to the fault location, which is determined by the highest probability $\max(p_a(k), p_b(k), p_c(k))$.
8:   Evaluate the transformations in (8b) and (8c) followed by (17a) and (17b).
9:   Execute a step of the algorithm [24] to get the current estimation of $\Theta_f(k)$. Compute $x_f(R_f = 0\,\Omega)$ from Θ_f, using (2a), and the known n_s and n_p.
10: **end while** .

---

winding architecture with n_p parallel branches and n_s coils in series, as detailed in Section II, the algorithm can accommodate various concentrated motor configurations. Furthermore, the proposed algorithm applies even to motors with distributed windings. However, the values of the constants n_p and n_s cannot be determined through the visual examination of the stator winding, requiring estimation. The identification procedure is executable in an experiment featuring the known fault severity x_f and short-circuit resistance R_f. In this experiment, Algorithm 3 is modified to compute n_p and n_s in Step 9 instead of calculating the recognized fault indicators.

Although the diagnostic method is formulated using the simplified model where $L_d = L_q = L_s$, it remains applicable to motors with differing $d-q$ inductances, provided the difference is not excessively large ($L_d < 1.2L_q$). In this case, the identified L_s value corresponds to the average of the $d-q$ inductances, and the fault indicators estimator associates the higher odd harmonics of the fault current with the system noise. In the opposing scenario, the notable difference in the $d-q$ inductances introduces a bias into the estimates of the electrical parameters and fault indicators, which can be resolved only by employing more sophisticated discrete-time models recognizing $L_d \neq L_q$ [30]. However, relying on these models also mandates enhancement in the inputs' excitation.

By formulating the mathematical model of a shorted PMSM with a distinct healthy machine description and fault equation related to the ISC-containing phase, as presented in Section II, the diagnostic approach effortlessly adapts even to multiphase motors. In addition, due to the use of more phase currents in forming the $\alpha - \beta$ components, suppressing the system noise, particularly that from the current sensors, is more effective than in a three-phase motor. The improved noise mitigation allows for a more aggressive tuning of the parameter estimators in
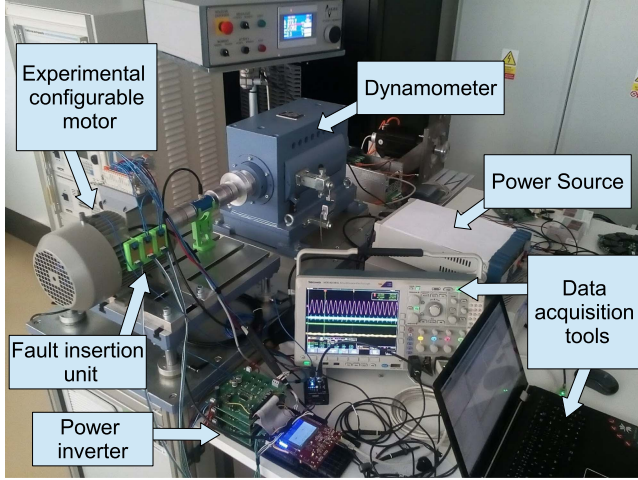
Fig. 3.   Diagnostic algorithm testing setup: The 200 W motor.

Motor (MCU)	Measured Time	Motor control	Data preproc.	Algorithm 1	Algorithm 2	Algorithm 3
200 W (TC277)	Min	12.6	1.0	28.6	51.0	53.2
	Average	14.4	1.2	29.8	52.7	54.8
	Max	16.2	1.5	30.4	54.5	60.1
20 kW (TC397)	Min	21.5	1.5	22.7	34.4	39.4
	Average	22.0	1.5	23.0	34.9	41.8
	Max	22.4	1.7	25.1	35.4	46.0

Algorithm 1 (higher values of the constrained terms Ξ and tuning factor ζ), ultimately ensuring superior sensitivity in fault detection. Conversely, the fault location identification, realized through the transformation in (14) and the probability assessment in (15), demands more phase shifts, leading to elevated computational requirements and a decelerated convergence of the probabilities p_j.

IV. VALIDATING THE DIAGNOSTIC ALGORITHM

The functioning of the diagnostic algorithm was validated by using a vector-controlled 200 W experimental motor with windings connected according to $n_p = 1$, $n_s = 3$, and 25 turns in one coil segment (75 turns in the whole winding). The diagnostic algorithm was implemented into an AURIX Application Kit TC277, controlling an NXP three-phase low-voltage power stage and operating with a sampling frequency of 10 kHz. An image of the testbed is displayed in Fig. 3.

The microcontroller TC277 has three independent 32-bit TriCore CPUs. Each core works at a frequency of 200 MHz and has its own floating-point unit supporting single precision operations. Microcontrollers with similar computing powers are now commonly available (for instance, the SPC5, STM32H7, TMS320F2837xD, and RH850/E2x) and can be used in motor applications. The control algorithm is integrated into the first core of the microcontroller. Triggered by an interrupt from the A/D converters, the control algorithm utilizes the measured abc currents and rotor position as the inputs and provides the updated duty cycles and internal variables (i_α, i_β, u_α, u_β, $\sin(\theta_e)$, $\cos(\theta_e)$, and $\bar{\omega}_e$), required by the diagnostic algorithm, as the outputs.

The second core, reserved for the diagnostic procedure, receives an interrupt emitted by the first core after the control algorithm step has been executed. The first core continues with duty-cycle updating, while the second one copies the input variables into the local ones and starts the fault diagnostic procedure. The diagnostic function was prepared to be calculated in single precision. During the implementation, we carefully analyzed the crucial calculation segments involving the addition

or subtraction of numbers with varying orders of magnitude, leading to a loss in the computational accuracy. Notably, an accurate evaluation of the logarithms and reciprocal values of the numbers in close proximity to one is especially critical; thus, we decided to approximate these problematic functions by their Taylor series of the fourth order close to point 1, effectively resolving the abovementioned problem. The presented modifications allowed the diagnostic algorithm to be implemented in the target microcontroller using only one core. Regarding the computational time, the combination of Algorithms 1 and 2 uses one microcontroller core at 83%–88%. Subsequently, the average microcontroller load decreases to 55%–62% after fault detection, as only Algorithm 3 is computed. Table I lists the computational times achieved through the algorithm implementation on the TC277 and TC397 microcontrollers.

The third core facilitates communication and data acquisition. The essential data from the microcontroller are transferred via Ethernet; simultaneously, Ethernet serves as the conduit for sending the control commands to the system. The AURIX sends a UDP packet with 400 data bytes every sampling period; considering the necessary headers, this represents a data flow of 4.64 MB/s. Such communication allows real-time monitoring of 100 distinct numerical values.

An ISC is emulated using a fault insertion unit (see Fig. 3) with an antiseries arrangement of two PSMNR90-50SLH MOSFET power transistors and an ACS709 current sensor to measure the fault current. Assuming the characteristics of the utilized components, an ISC is emulated with a short-circuit resistance of $2.5\,\text{m}\Omega$. However, the resulting short-circuit current is also affected by the inductance of the wires linking the motor and fault insertion unit, which is not negligible compared with the inductance of one or two turns in the experimental motor winding.

In the initial part of the validation experiments, we assessed the functionality of our method (including the estimation of the electrical parameters) under both the steady and the transient state conditions. The outcomes are depicted in Fig. 4 above. The experimental motor was driven to the angular velocity setpoint, and the ISCs were emulated in phase a with the fault severity of 4/25 using the fault insertion unit. Simultaneously, the dynamometer exerted a torque load consistent at 0.5 Nm (steady state and velocity transient) or gradually rising from 0.25 to 0.75 Nm, with a 2 Nm/s rate (load transient).

As shown in Fig. 4, even though the persistence of the input signals diminishes rapidly during the steady state, the parametric
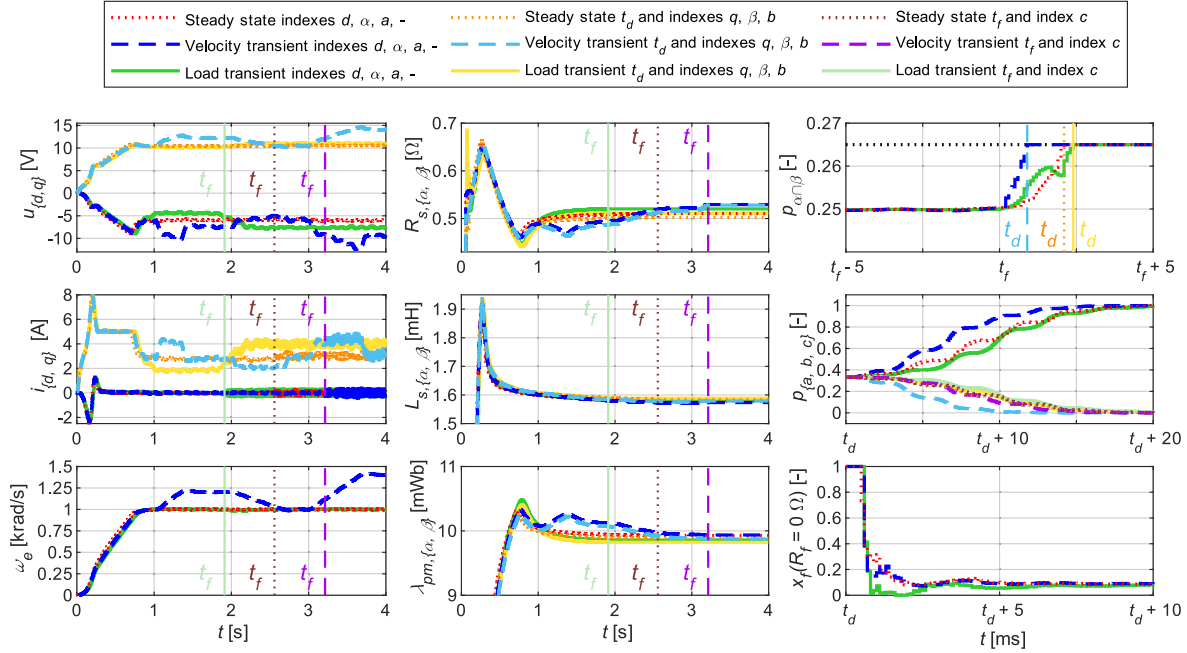
Fig. 4. Estimated electrical parameters, fault indicators, and fault detection-related waveforms: The 200 W motor.

estimation algorithm can preserve the information obtained during the transients to produce stabilized and smoothened estimations of the motor's electrical parameters. Furthermore, the persistence requirements in the steady state can be effectively lowered by utilizing the previously recognized permanent magnet flux linkage as a constant. As also visualized in Fig. 4, the implemented algorithm is capable of tracking changes in the time-varying electrical parameters of the experimental motor, including minor increases in the resistance of the stator winding and MOSFET power transistors due to heating. The emulated fault, occurring at the time t_f, is then detected at the time t_d within 3 ms. Generally, a higher amplitude of the currents and an elevated angular velocity lead to a faster detection. In the load transient, however, the detection might decelerate compared to the steady state scenario assuming the same current level; this is because the detection utilizes the electrical parameters that are concurrently updated and whose estimates remain unsettled. The fault indicators are then recognized within 6 ms after the detection at t_d.

In the subsequent part of the validation experiments, we tested the diagnostic capabilities of the designed algorithm across the different operating conditions (steady state without a load, load transient with a 5 Nm/s rate, and velocity transient without a load) and emulated fault severities (2/25, 4/25, and 6/25). The observed outcomes are exposed in Fig. 5 below, where, at the angular velocity of $\omega_e = 1200$ rad/s, the diagnostic algorithm detects even two shorted turns, approximately corresponding to the converted value $x_f(R_f = 0\,\Omega) = 0.04$, which represents 1.33% of the entire stator winding shorted with a zero resistance. Despite the experimental motor's potential for a maximum electrical angular velocity of 10^4 rad/s, the validation experiments were intentionally carried out at a moderated rate

because detecting ISCs is especially challenging at lower angular velocities, attributable to the diminished back-electromotive force and resulting lower fault current amplitude. The value $\omega_e = 1200$ rad/s proved to be the minimum velocity at which the detection algorithm can reliably detect two shorted turns of the unloaded motor. Detecting two shorted turns at lower rates would require tuning the electrical parameter estimators more aggressively (higher values of Ξ and ζ in Algorithm 1). However, as the experimental motor exhibits an asymmetry in the stator windings (see Fig. 5, where the second harmonic distortion in the $d - q$ currents is observable even before a short-circuit occurs), adopting a more aggressive tuning would result in a false detection of this asymmetry at higher velocity rates and also in other issues related to the rapid loss of the information learned about the electrical parameters.

As shown in Fig. 5, applying a higher load to the 200 W motor yields an increased q-axis current, producing an elevated signal-to-noise ratio and thus a faster detection and estimation of the fault indicators; such properties are obtained despite the faults occurring in the load transient. During the velocity transient experiments, the ISCs were emulated close to 1100 rad/s at a change from 800 to 1200 rad/s. Stabilizing the fault severity and location, as evidenced in Fig. 5, takes more time: the velocity is lower than in the steady state scenario, leading to a decreased rate of change in the $\alpha - \beta$ voltages and currents.

In order to substantiate the functionality and effectiveness of the proposed diagnostic algorithm across different machine designs, we applied our method even to another experimental motor with a rated power of 20 kW and maximum electrical angular velocity of 1.1×10^4 rad/s. The testbed featuring the 20 kW motor is visualized in Fig. 6.
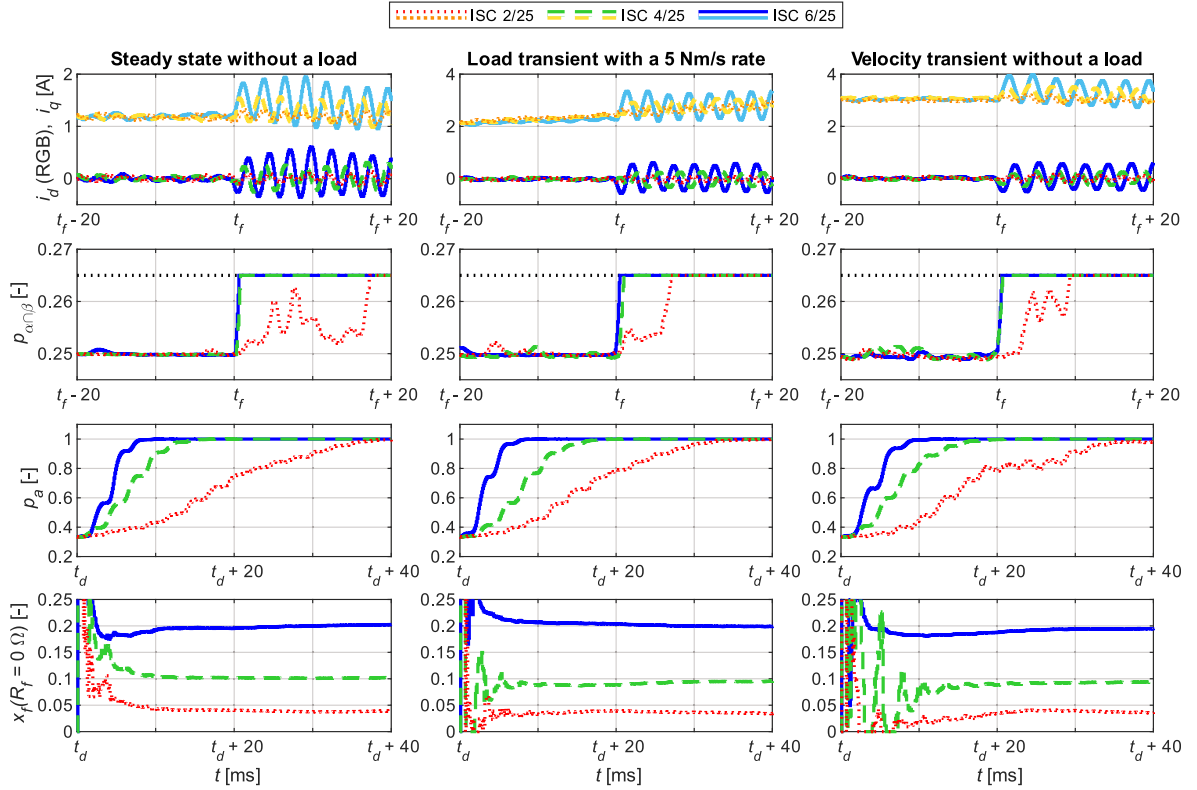
Fig. 5.   Testing the algorithm's capabilities under the different operating conditions and fault severities: The 200 W motor.
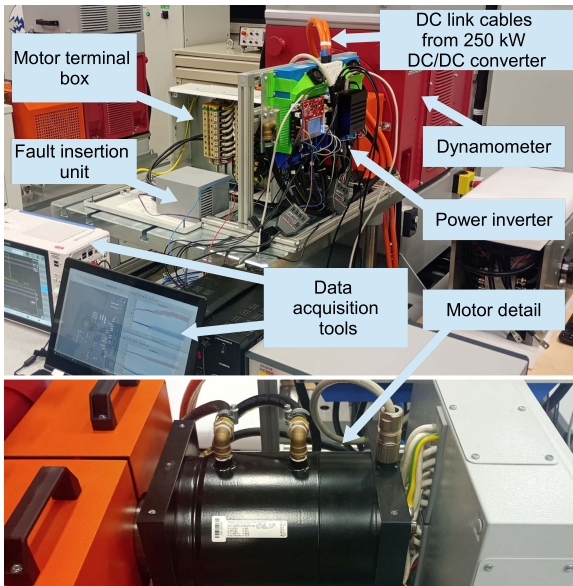

Fig. 6.   Diagnostic algorithm testing setup: The 20 kW motor.

Fig. 7.   Gradually arising fault current in a case with a 10 Nm load.

The stator windings of the 20 kW motor, driven by an Infineon HYBRID KIT DRIVE power stage with an AURIX Application Kit TC397 at a sampling rate of 10 kHz, comprise two parallel branches, each containing two coil segments arranged in series ($n_p = 2$ and $n_s = 2$); a part contains seven turns. The estimated electrical parameters are $R_s = 6.05\,\mathrm{m\Omega}$, $L_s = 90.2\,\mu\mathrm{H}$, and $\lambda_{\mathrm{pm}} = 11.7\,\mathrm{mWb}$.

Although the target microcontroller has six cores operating at 300 MHz, only three were used, as in the previous case. The first core is dedicated to the control algorithm, which contains many safety and self-monitoring features, unlike the first implementation, where only a speed controller and $d - q$ current controllers were implemented. The control algorithm also includes a state machine managing the startup sequence and zero calibration of the current sensors. The proposed diagnostic algorithm runs in the second core, while the communication is implemented in the third one. The synchronization between the cores is the same as in the TC277 implementation. The measured computational times of the diagnostic algorithm in Table I above reflect the increased computational power of the microcontroller, although the execution of the control algorithm runs longer, considering its increased complexity.
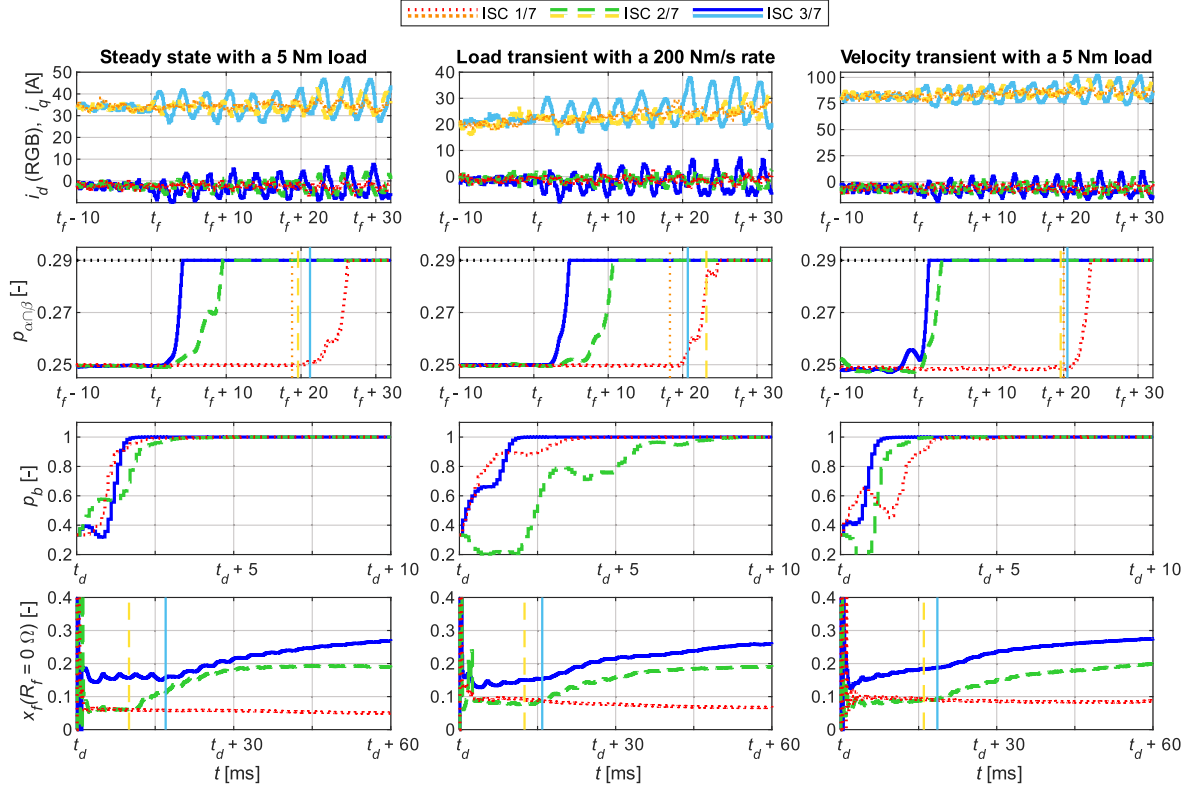
Fig. 8. Testing the algorithm's capabilities under the different operating conditions and fault severities: The 20 kW motor.

Unlike the 200 W machine discussed above, the 20 kW motor operates with higher voltages, currents, and noise levels of the current sensors. We therefore performed more robust tuning of the electrical parameter estimators ($\Xi = 0.1\,\mathbf{I}^{3\times3}$ and $\zeta = 0.1$ in Algorithm 1) and the fault detector ($\xi = 0.04$ in Algorithm 2). Furthermore, we implemented adaptive band-pass filters of i_α, i_β, u_α, u_β, v_α, and v_β to suppress the occasionally occurring outlier values caused by an interference from the devices surrounding the motor. We have

$$y(k+1) = b\big(u(k) - u(k-1)\big) + a_1 y(k) + a_2 y(k-1)$$

$$b = 2\frac{\psi}{\sqrt{1-\psi^2}}e^{-\psi\omega_e(k)T_s}\sin\big(\omega_e(k)T_s\sqrt{1-\psi^2}\big)$$

$$a_1 = 2e^{-\psi\omega_e(k)T_s}\cos\big(\omega_e(k)T_s\sqrt{1-\psi^2}\big)$$

$$a_2 = -e^{-2\psi\omega_e(k)T_s} \qquad (18)$$

where $u(k)$ and $y(k)$ are the filter input and output, respectively, and the damping factor ψ is set to 0.3.

An ISC in the 20 kW motor is emulated using a fault insertion unit (see Fig. 6) comprising a power relay LEV200A4NAF connected in parallel to a power module sTT1400N16P55 with two antiparallel thyristors. A control signal is then simultaneously dispatched to the relay and thyristors. However, due to the mechanical movement, the relay reaction is delayed by 20 $\pm$ 5 ms compared with the thyristors' response, resulting in an extended relay lifespan. On the other hand, the fault gradually arises in two steps with a relative shift, attributed to a voltage drop on the thyristors (0.85–1.39 V), which also decreases the

fault current at a low-fault severity. The described situation is shown in Fig. 7, which displays the measured fault currents. The vertical lines in Figs. 7 and 8 below are attributed to the time t_{fr} when the relay is switched ON.

The second experimental motor was driven to the ω_e setpoint of 1000 rad/s, and the ISCs were emulated in phase b with different fault severities (1/7, 2/7, and 3/7) and loads generated by the dynamometer (consistent 5 Nm or a gradual rise from 2 to 7 Nm, with a rate of 200 Nm/s). In the velocity transient experiments, the faults were emulated close to 1100 rad/s (velocity change from 1000 to 1400 rad/s). The outcomes of the fault detection and indicator estimation experiments are depicted in Fig. 8 below, indicating that higher fault severity values are detected even before the relay activation. Subsequently, the fault severity estimator follows the value associated with the lower fault current, and after the relay has been switched ON, the estimator adapts to the increased value of i_f. As the velocity increases in the relevant transient experiments, the ISCs are detected faster, and the fault location and severity estimations are accelerated.

V. CONCLUSION

This article proposed model-based fault diagnostics for synchronous motors with permanent magnets under an ISC fault. The designed algorithm allowed detecting the fault and estimated its location and severity using parametric estimation and model comparison approaches expanded to include probabilistic fault detection. In the table below, the essential properties of the

TABLE II
COMPARING THE FAULT SEVERITY ESTIMATION APPROACHES

Examined property	Designed method	[15]	[16]	[17]	[18]	[19]	[20]	[21]
Detecting fault occurrence	✓	✓	✓	✗	✗	✗	✓	✓
Estimating fault location	✓	✓	✓	✗	✗	✗	✓	✗
Functioning in transient states	✓	✗	✗	✗	✗	✗	?	✓
Adapting to the current operating point	✓	✓	✓	✗	✗	✗	✓	✓
Exclusively based on control structure signals	✓	✗	✓	✓	✓	✓	✗	✓
Computationally efficient	✓	✓	✗	✓	✓	✓	✓	?
Tolerating large difference of $d-q$ inductances	✗	✗	✓	✗	✗	✗	?	✓

designed method were compared with other severity estimation options.

As shown in Table II, the neural network-based method [21] also satisfied most of the modern diagnostics requirements. The technique, however, required collecting the training data for a number of operating points and fault severities, meaning that the targeted healthy motors must have intentionally shorted before the abovementioned principle was applied. By contrast, the designed algorithm recursively learnt the running motor's electrical parameters before a short-circuit occurred, and the fault-related characteristics were recognized throughout the parametric estimation of the universal fault model after the fault detection. Furthermore, since the learning procedure ran long before a fault occurred, the detection was robust to the system noise and applied even to different types of faults that were trackable from the electrical signals and to the general class of models reproducing the Normal–Wishart probability distribution. In addition, our algorithm allowed identifying the fault location and was successfully implemented into two motor control units without additional hardware extensions.

The main drawback lied in the limited applicability, as the method was usable only in machines with comparable rotor reference frame inductances. This aspect needed to be revised to eliminate significant biases in the estimated characteristics. Our future research will focus on expanding the parametric estimation and fault diagnostics to subsume motors with differing rotor reference frame inductances.

ACKNOWLEDGMENT

REFERENCES

[1] Y. Qi, E. Bostanci, V. Gurusamy, and B. Akin, "A comprehensive analysis of short-circuit current behavior in PMSM interturn short-circuit faults," *IEEE Trans. Power Electron.*, vol. 33, no. 12, pp. 10784–10793, Dec. 2018, doi: 10.1109/TPEL.2018.2809668.

[2] M. Krzysztofiak, M. Skowron, and T. Orlowska-Kowalska, "Analysis of the impact of stator inter-turn short circuits on PMSM drive with scalar and vector control," *Energies*, vol. 14, no. 1, Dec. 2020, Art. no. 153, doi: 10.3390/en14010153.

[3] Z. Gao, C. Cecati, and S. X. Ding, "A survey of fault diagnosis and fault-tolerant techniques—Part I: Fault diagnosis with model-based and signal-based approaches," *IEEE Trans. Ind. Electron.*, vol. 62, no. 6, pp. 3757–3767, Jun. 2015, doi: 10.1109/TIE.2015.2417501.

[4] T. Orlowska-Kowalska et al., "Fault diagnosis and fault-tolerant control of PMSM drives-state of the art and future challenges," *IEEE Access*, vol. 10, pp. 59979–60024, 2022, doi: 10.1109/ACCESS.2022.3180153.

[5] B. Cai, Y. Zhao, H. Liu, and M. Xie, "A data-driven fault diagnosis methodology in three-phase inverters for PMSM drive systems," *IEEE Trans. Power Electron.*, vol. 32, no. 7, pp. 5590–5600, Jul. 2017, doi: 10.1109/TPEL.2016.2608842.

[6] A. M. da Silva, R. J. Povinelli, and N. A. O. Demerdash, "Induction machine broken bar and stator short-circuit fault diagnostics based on three-phase stator current envelopes," *IEEE Trans. Ind. Electron.*, vol. 55, no. 3, pp. 1310–1318, Mar. 2008, doi: 10.1109/TIE.2007.909060.

[7] P. Pietrzak, M. Wolkiewicz, and T. Orlowska-Kowalska, "PMSM stator winding fault detection and classification based on bispectrum analysis and convolutional neural network," *IEEE Trans. Ind. Electron.*, vol. 70, no. 5, pp. 5192–5202, May 2023, doi: 10.1109/TIE.2022.3189076.

[8] X. Li, W. Zhang, N.-X. Xu, and Q. Ding, "Deep learning-based machinery fault diagnostics with domain adaptation across sensors at different places," *IEEE Trans. Ind. Electron.*, vol. 67, no. 8, pp. 6785–6794, Aug. 2020, doi: 10.1109/TIE.2019.2935987.

[9] M. A. Mazzoletti, G. R. Bossio, C. H. De Angelo, and D. R. Espinoza-Trejo, "A model-based strategy for interturn short-circuit fault diagnosis in PMSM," *IEEE Trans. Ind. Electron.*, vol. 64, no. 9, pp. 7218–7228, Sep. 2017, doi: 10.1109/TIE.2017.2688973.

[10] J.-C. Urresty, J.-R. Riba, and L. Romeral, "Diagnosis of interturn faults in PMSMs operating under nonstationary conditions by applying order tracking filtering," *IEEE Trans. Power Electron.*, vol. 28, no. 1, pp. 507–515, Jan. 2013, doi: 10.1109/TPEL.2012.2198077.

[11] S. Huang, A. Aggarwal, E. G. Strangas, B. Khoshoo, K. Li, and F. Niu, "Mitigation of interturn short-circuits in IPMSM by using MTPCC control adaptive to fault severity," *IEEE Trans. Power Electron.*, vol. 37, no. 4, pp. 4685–4696, Apr. 2022, doi: 10.1109/TPEL.2021.3127538.

[12] F. Chen, J. Fan, W. Li, J. Fang, and S. Ding, "Mitigation of high-resistance connection in surface-mounted PMSM drive system based on model predictive current control," *Results Eng.*, vol. 15, Sep. 2022, Art. no. 100590, doi: 10.1016/j.rineng.2022.100590.

[13] J. Zhang, W. Zhan, and M. Ehsani, "Fault-tolerant control of PMSM with inter-turn short-circuit fault," *IEEE Trans. Energy Convers.*, vol. 34, no. 4, pp. 2267–2275, Dec. 2019, doi: 10.1109/TEC.2019.2936225.

[14] I. Jeong, B. J. Hyon, and K. Nam, "Dynamic modeling and control for SPMSMs with internal turn short fault," *IEEE Trans. Power Electron.*, vol. 28, no. 7, pp. 3495–3508, Jul. 2013, doi: 10.1109/TPEL.2012.2222049.

[15] J. Hang, D. Yan, M. Xia, S. Ding, and Q. Wang, "Quantitative fault severity estimation for high-resistance connection in PMSM drive system," *IEEE Access*, vol. 7, pp. 26855–26866, 2019, doi: 10.1109/ACCESS.2019.2901121.

[16] B. M. Ebrahimi and J. Faiz, "Feature extraction for short-circuit fault detection in permanent-magnet synchronous motors using stator-current monitoring," *IEEE Trans. Power Electron.*, vol. 25, no. 10, pp. 2673–2682, Oct. 2010, doi: 10.1109/TPEL.2010.2050496.

[17] Y. Qi, E. Bostanci, M. Zafarani, and B. Akin, "Severity estimation of interturn short circuit fault for PMSM," *IEEE Trans. Ind. Electron.*, vol. 66, no. 9, pp. 7260–7269, Sep. 2019, doi: 10.1109/TIE.2018.2879281.

[18] Z. Zeng, M. Zhang, L. Chen, Q. Huang, and D. Sun, "A new method to estimate the severity of interturn short-circuit fault for PMSM," in *Proc. IEEE Int. Conf. Power Syst. Technol.*, 2022, pp. 149–154, doi: 10.1109/PSET56192.2022.10100348.

[19] Y. Qi, M. Zafarani, V. Gurusamy, and B. Akin, "Advanced severity monitoring of interturn short circuit faults in PMSMs," *IEEE Trans. Transport. Electrific*, vol. 5, no. 2, pp. 395–404, Jun. 2019, doi: 10.1109/TTE.2019.2913357.

[20] X. Liu, W. Miao, Q. Xu, L. Cao, C. Liu, and P. W. T. Pong, "Inter-turn short-circuit fault detection approach for permanent magnet synchronous machines through stray magnetic field sensing," *IEEE Sensors J.*, vol. 19, no. 18, pp. 7884–7895, Sep. 2019, doi: 10.1109/JSEN.2019.2918018.

[21] H. Lee, H. Jeong, G. Koo, J. Ban, and S. W. Kim, "Attention recurrent neural network-based severity estimation method for interturn short-circuit fault in permanent magnet synchronous machines," *IEEE Trans. Ind. Electron.*, vol. 68, no. 4, pp. 3445–3453, Apr. 2021, doi: 10.1109/TIE.2020.2978690.

[22] S. Bachir, S. Tnani, J.-C. Trigeassou, and G. Champenois, "Diagnosis by parameter estimation of stator and rotor faults occurring in induction machines," *IEEE Trans. Ind. Electron.*, vol. 53, no. 3, pp. 963–973, Jun. 2006, doi: 10.1109/TIE.2006.874258.

[23] S. Moon, H. Jeong, H. Lee, and S. W. Kim, "Interturn short fault diagnosis in a PMSM by voltage and current residual analysis with the faulty winding model," *IEEE Trans. Energy Convers.*, vol. 33, no. 1, pp. 190–198, Mar. 2018, doi: 10.1109/TEC.2017.2726142.

[24] J. Dokoupil and P. Václavek, "Regularized estimation with variable exponential forgetting," in *Proc. 59th IEEE Conf. Decis. Control*, 2020, pp. 312–318, doi: 10.1109/CDC42340.2020.9304385.

[25] J. Dokoupil, M. Papež, and P. Václavek, "Comparison of Kalman filters formulated as the statistics of the normal-inverse-Wishart distribution," in *Proc. IEEE 54th Conf. Decis. Control*, 2015, pp. 5008–5013, doi: 10.1109/CDC.2015.7403002.

[26] J. Dokoupil, A. Voda, and P. Václavek, "Regularized extended estimation with stabilized exponential forgetting," *IEEE Trans. Autom. Control*, vol. 62, no. 12, pp. 6513–6520, Dec. 2017, doi: 10.1109/TAC.2017.2656379.

[27] J. Dokoupil and P. Václavek, "Variable exponential forgetting for estimation of the statistics of the Normal-Wishart distribution with a constant precision," in *Proc. IEEE 58th Conf. Decis. Control*, 2019, pp. 5094–5100, doi: 10.1109/CDC40024.2019.9029290.

[28] T. Söderström and P. Stoica, *System Identification*. Uppsala, Sweden: Prentice Hall Int., 2001, ISBN 0-13-881236-5.

[29] L. Zezula, "Fault relevance diagnostics of the PMSM under the inter-turn short circuit fault," Master's Thesis, Fac. Elect. Eng. Commun., Dept. Control Instrum., Brno Univ. Technol., Brno, Czech Republic, 2022.

[30] L. Zezula and P. Blaha, "Discrete-time modeling of PMSM for parametric estimation and model predictive control tasks," in *Proc. IECON 49th Annu. Conf. IEEE Ind. Electron. Soc.*, 2023, pp. 1–6, doi: 10.1109/IECON51785.2023.10312226.

Matus Kozovsky received the Ph.D. degree in cybernetics from the Brno University of Technology, Brno, Czech Republic, in 2021.

He is currently a Researcher of SW development with the Central European Institute of Technology, Brno University of Technology. His research interests include the fault-tolerant control of ac electric motors, high-speed control of electrical motors, and inverter SW improvements.

Petr Blaha received the M.Sc. degree in cybernetics, control and measurements and Ph.D. degree in cybernetics and informatics from the Brno University of Technology, Brno, Czech Republic, in 1996 and 2001, respectively. He is currently a Senior Researcher with the Central European Institute of Technology, Brno University of Technology, Brno, Czech Republic. Since 2007, he has been an Associate Professor with the Brno University of Technology. His research interests include the parameter identification and advanced control of ac electric motors and the fault tolerant control of electrical motor drives.

Lukas Zezula received an M.Sc. in cybernetics, control and measurements from the Brno University of Technology, Brno, Czech Republic, in 2022. He is currently working toward the Ph.D. degree.

He is currently a Research Assistant with the Central European Institute of Technology, Brno University of Technology. His research interests include the continuous and discrete-time modeling of ac machines under failures and diagnostics in ac electric motors.